Sterically driven current reversal in a molecular motor model

Alex Albaugh[a,b], Geyao Gu[a], and Todd R. Gingrich[a,1]

Simulations can help unravel the complicated ways in which molecular structure determines function. Here, we use molecular simulations to show how slight alterations of a molecular motor's structure can cause the motor's typical dynamical behavior to reverse directions. Inspired by autonomous synthetic catenane motors, we study the molecular dynamics of a minimal motor model, consisting of a shuttling ring that moves along a track containing interspersed binding sites and catalytic sites. The binding sites attract the shuttling ring while the catalytic sites speed up a reaction between molecular species, which can be thought of as fuel and waste. When that fuel and waste are held in nonequilibrium steady-state concentrations, the free energy from the reaction drives directed motion of the shuttling ring along the track. Using this model and nonequilibrium molecular dynamics, we show that the shuttling ring's direction can be reversed by simply adjusting the spacing between binding and catalytic sites on the track. We present a steric mechanism behind the current reversal, supported by kinetic measurements from the simulations. These results demonstrate how molecular simulation can guide future development of artificial molecular motors.

molecular motors | molecular dynamics | computational chemistry | statistical mechanics

Molecular motors generate directed motion by harnessing free energy gradients, harvested, for example, from the hydrolysis of adenosine triphosphate (ATP) into adenosine diphosphate (ADP) and inorganic phosphate (P_i) (1–3). That directed motion has an essential biological function—dynein and kinesin transport molecular cargoes on microtubules (4, 5), myosin walks along the actin to drive muscle contraction (6), and ATP synthase links rotary motion to chemical synthesis (7). The fuel consumption enables directional motion, but the thermodynamic driving force does not fully determine the direction of that motion. Most myosins hydrolyze ATP to walk along an actin track from − to +, but myosin VI uses the same thermodynamic drive to walk in the opposite direction (8). This feature gives myosin VI unique and important biological function (9), so significant effort has been devoted to understanding the structural basis for the reversed motion (10). Similar studies have examined the structural basis for directionality in kinesin (11) and dynein (12).

Although recent breakthroughs in synthetic chemistry have led to artificial autonomous chemically fueled molecular motors (13–15), it remains a challenge to achieve a similar level of directional control in those designed motors. The motion of nonautonomous machines driven by magnetic fields (16, 17) can be flipped by inverting the field, but inverting the driving force is less desirable for a chemically fueled autonomous machine. As in the myosin examples, even without altering the fuel and its thermodynamic driving force, it should be possible to introduce structural changes to move in the opposite direction. Engineering those structural changes is challenged by the fluctuations exhibited in nanoscale motion (18, 19), which prevent molecular motors from executing deterministic mechanisms like their macroscopic counterparts. We therefore must differentiate between three types of reversed motion: i) a fluctuation that causes a motor of a fixed design to spontaneously move in opposition to its typical behavior (20), ii) a reversal of the typical behavior of a fixed design due to a negated thermodynamic drive (21), and iii) a reversal of the typical behavior by altering a motor design without altering the drive. Here, we report this final type of reversal in a simulation model (22) inspired by the catenane motor of Wilson et al. (13).

That catenane motor, an experimental realization of an autonomous synthetic chemically fueled motor, consists of two interlocked rings. The larger of the two rings can be viewed as a track around which the smaller randomly diffuses. Wilson et al. showed that by coupling the supramolecular complex to a chemical reaction (the conversion of 9-fluorenylmethoxycarbonyl chloride into dibenzofulvene and carbon dioxide), the diffusion of the smaller shuttling ring can be gated to statistically prefer clockwise motion. Two of us used that essential design to construct a molecular dynamics model of a catenane-like motor that is similarly coupled to a fuel decomposition (22). Like the

Significance

Biophysical motors convert chemical energy to useful work at the molecular scales. Due to breakthroughs in synthetic chemistry, those biological motors have now been joined by artificial motors that similarly harvest energy from chemical fuel to move. In this work, we use computer simulations to identify how the structure of such a synthetic motor relates to its direction of motion. In particular, we find that the spacing between motor components causes key steric interactions that determine whether the motor moves forward or backward. Uncovering design principles like this will be important when building future iterations of artificial molecular motors.

Author affiliations: [a]Department of Chemistry, Northwestern University, Evanston, IL 60208; and [b]Department of Chemical Engineering and Materials Science, Wayne State University, Detroit, MI 48202

[1]To whom correspondence may be addressed. Email: todd.gingrich@northwestern.edu.

experimental system, that model consisted of two repeated copies of a motif around the large ring. These motifs are composed of a binding site that attracts the shuttling ring and a catalytic site where the decomposition reaction is catalyzed. By introducing grand canonical Monte Carlo (GCMC) moves into the simulation, a nonequilibrium steady state (NESS) is sustained in which fuel is typically added, a decomposition reaction is catalyzed through an interaction with the motor, and the waste products are removed. The NESS presents the motor with a replenishing supply of high-free-energy fuel whose decomposition can be coupled to directed motion.

While holding fixed the fuel's driving force, we here show that the direction of the motor is reversed by increasing the number of repeated motifs around a shuttling ring of a fixed size. Upon translating the rotary motor into a linear one, we demonstrate that the reversal arises from the spacing between binding and catalytic sites within the repeated motifs. The shuttling ring at a binding site sterically repels fuel molecules from accessing nearby catalytic sites, and the kinetics of shuttling ring motion flips depending on whether the steric repulsion occludes the nearest catalytic site or the two nearest sites. We present that argument at a schematic level and validate it by measuring the rate of key kinetic steps from the NESS simulations. In addition to informing the design of experimentally realized catenane motors, our results emphasize how sensitively dynamic function can depend on molecular design.

Results

A Rotary Motor. The catenane motors upon which this work is built consist of two motifs on opposite sides of a large ring (13, 22). Those motifs contain adjacent components that bind a shuttling ring and catalyze a reaction. The regions between motifs are inert, and are represented as volume-excluding particles that serve as an essentially featureless track. Along that track, the shuttling ring diffuses, but the blocking and unblocking of the

catalytic sites generate directionality by gating the diffusion in a manner that has been interpreted as an information ratchet (23). One may therefore view each motif like a tooth on a ratchet, offering a means to lock in the shuttling ring's forward progress. That picture suggests that adding more teeth would make it easier to prevent incremental progress from backsliding, thereby amplifying the current, e.g., the rate of net clockwise hops. We therefore hypothesized that increasing the number of motifs while maintaining the size of the large ring would make a better motor that pushes the shuttling ring in a preferred clockwise direction more efficiently with higher current. A previous study showed that creating [2]-catenanes with more than two shuttling ring binding sites is possible (24), making this an experimentally realizable configuration. Fig. 1 shows that our intuition about teeth on a ratchet was spectacularly wrong. There, we show results from NESS simulations (22) with a varying number of the motifs, reflecting that the addition of motifs can actually induce current to reverse directions.

Briefly, the simulations introduce a classical cluster of Lennard–Jones particles we call a full tetrahedral cluster (FTC) which, over the course of Langevin dynamics, can decompose into an empty tetrahedral cluster (ETC) and a central particle (C) that had been stuck inside the full cluster (25). This reversible decomposition reaction is held away from equilibrium by three separate GCMC chemostats, one each for FTC, ETC, and C. As pictured, the motifs, spaced as evenly as possible around the large ring, each consist of a single orange particle acting as a binding site next to three white particles acting as a catalytic site. Details of the attractions and repulsions between particles are discussed in *Materials and Methods*. The interlocked rings undergo translational and rotational diffusion within the simulation box, but we focus on the diffusion of the shuttling ring along the track of the large ring. We measure that current by monitoring which particle along the large ring is closest to the center of mass of the shuttling ring and by recording when the shuttling ring hops clockwise (CW) or counterclockwise (CCW)
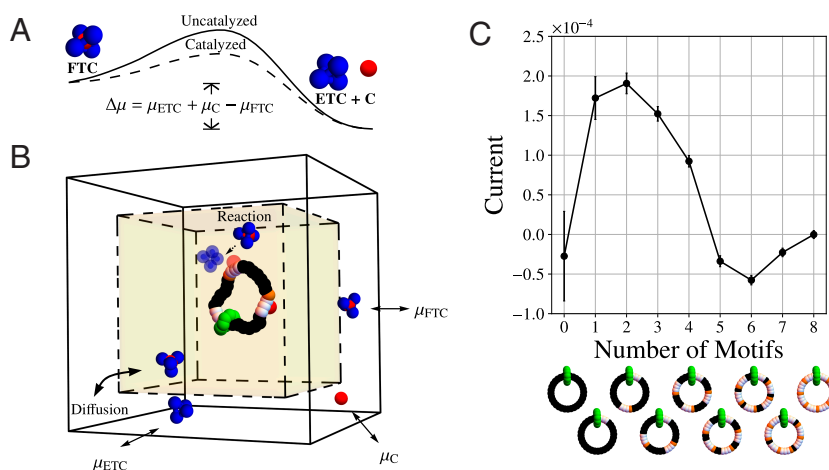

Fig. 1. (*A*) The decomposition of a full tetrahedral cluster (FTC) into an empty tetrahedral cluster (ETC) and free central particle (C) provides a thermodynamic driving force to power a molecular motor. (*B*) That rotary motor comprises a small shuttling ring (green) that diffuses around a larger ring. The larger ring has repeated motifs consisting of a site that binds the shuttling ring (orange particle) and an adjacent catalytic site (a cluster of three neighboring white particles) that catalyzes the FTC decomposition. As described in ref. 22, the motor is simulated under nonequilibrium steady state (NESS) conditions associated with a surplus of FTC. A periodic-boundary-condition simulation box is divided into a yellow motor-containing region, modeled by Langevin dynamics, and an exterior white region which supplements the Langevin dynamics with grand canonical Monte Carlo chemostats to hold FTC, ETC, and C species at the respective chemical potentials, μ_{FTC}, μ_{ETC}, and μ_C. Provided diffusion between the two regions is sufficiently fast, the motor's dynamics sample a NESS with a thermodynamic driving force generated by those chemostats. (*C*) While fixing the large ring to have 32 particles, the number of repeated motifs was varied from zero to eight, with volume-excluding, inert black particles separating those motifs. The average current (net clockwise hops per time) reverses from positive to negative as more motifs are added. Data points and error bars are given by the mean and standard error across 100 independent simulations with 2×10^8 time steps of size $\Delta t = 5 \times 10^{-3}$.

by one particle. Integrating those hops over a simulation with N_{steps} and time step Δt gives a net number of clockwise hops Δn observed in time $\tau \equiv N_{steps}\Delta t$. A net hops-per-time current is thus reported as $j = \Delta n/\tau$.

Here, we considered a ring with 32 total particles, so anywhere between zero and eight motifs could fit around the ring. A motor with either zero or eight motifs is symmetric, requiring the current to vanish in both cases. In between the extremes, Fig. 1C shows the current rises and falls—the original 2-motif catenane design moves CW while a motor with 5, 6, or 7 motifs gives CCW currents.

A Linear Motor. Changing the number of motifs affects not only the number of teeth for a ratchet but also the spacing between a binding site and the catalytic site to the CCW direction. To study the importance of that spacing, we transformed the rotary motor of Fig. 1B into the linear motor of Fig. 2A, with a dynamic shuttling ring and a fixed periodic track. Such a linear configuration was suggested in ref. 26. Because of the periodic boundary conditions, our linear motor is still effectively a catenane. The linear geometry, however, eliminates curvature effects while allowing us to systematically change the spacings between adjacent binding and catalytic sites by varying the

Fig. 2. (A) The rotary motor of Fig. 1 is unfurled into a linear motor with periodic boundary conditions and with orange binding sites separated from white catalytic sites by l_1 and l_2 inert black particles. The box width was varied along with l_1 and l_2 to simulate a fixed track containing three motifs. Chemical potentials were imposed in the white region of the simulation box as in Fig. 1. (B) The steady-state current as a function of l_1 and l_2 was measured from 100 independent trajectories with 2×10^8 time steps of size $\Delta t = 5 \times 10^{-3}$. Current is trivially inverted by interchanging l_1 and l_2, but it is also nontrivially inverted along the slice with $l_2 = 0$ (dashed black line), consistent with the current reversal in Fig. 1. Data along that $l_2 = 0$ slice are highlighted below the heat map to illustrate the standard errors.

number of inert (black) particles to the *Left* (l_1) and *Right* (l_2) of each binding site. Fig. 2B shows a heat map of the current for a range of l_1 and l_2 spacings. Consistent with the rotary motor of Fig. 1, the direction depends on l_1 when $l_2 = 0$. Small l_1 gives CCW current while large l_1 flips to a CW current. By reproducing the current reversal in the linear model, we emphasize that the mechanism for the reversal arises from the spacings between catalytic and binding sites, not the number of motifs. This fact is further corroborated by *SI Appendix*, Fig. S2, where we show that the current of an $l_2 = 0$ linear motor is unaffected by the number of motifs.

A Steric Mechanism for Current Reversal. That the current reversal occurs when both l_1 and l_2 are small hints that it originates from a localized steric effect. The shuttling ring diffuses along the track but can be impeded when a C blocks the path by binding strongly to a catalytic site. The directionality of that gated diffusion thus depends on whether a C particle will tend to block the catalytic site to the left or right of the shuttling ring and whether the ring will stably rest at the neighboring binding sites. As we illustrate in Fig. 3, these effects can act in opposite directions, yielding the current reversal when $l_2 = 0$.

To understand that effect, first recognize that C blocks the shuttling ring by binding tightly to the catalytic site, but it can sometimes unbind to let the ring pass. Because the NESS operates under high-fuel, low-waste conditions, any C that randomly unbinds, is very likely to diffuse away from the motor and be extracted from the system. To reblock the catalytic site typically requires an FTC to decompose and leave a new C behind. Thus, the probability that a catalytic site is blocked depends sensitively on whether the site is accessible for an FTC to approach. Fig. 3, *Top Row* shows that steric repulsions between the shuttling ring and FTC can limit that accessibility on one side of the ring when l_1 is large (Fig. 3A) or on both sides when l_1 is small (Fig. 3B). Since the generation of blocking groups arises from FTC decomposition, the typical blocking group configurations (Fig. 3, *Bottom Row*) mirror the FTC accessibility. The positive current generated by the large l_1 motor in Fig. 3A straightforwardly follows from those typical blocked configurations; the shuttling ring can move to the right but not the left. Fig. 2 B, *Lower* also shows that the current does not plateau for large l_1, but continues to increase. This increase of the current at large l_1 arises due to the increasing distance between binding sites. The rate of net jumps between binding sites saturates at large l_1, but the current increases since the binding sites are further apart (*SI Appendix*, Fig. S8).

The situation becomes more nuanced when l_1 approaches the length scale of steric repulsions between FTC and the shuttling ring. In that case, catalytic sites to the left and right of the shuttling ring can both be unblocked. Although the shuttling ring can access the binding sites to the right and left, those sites are not equally stable because of the steric repulsions between the shuttling ring and blocking groups. Fig. 3 B, *Bottom Row* shows that those repulsions (red shaded region) will destabilize the rightward binding site more than the one on the left. Even if the ring were to make equal attempts to move left and right, the moves to the left would stick more often, yielding the net leftward motion.

We emphasize that the mechanisms for current in both directions depend on the nonequilibrium driving force. Were it not for the surplus of FTC, the system would obey detailed balance. FTC would still decompose into ETC and C, with C able to act as a blocking group at a catalytic site, but in equilibrium,
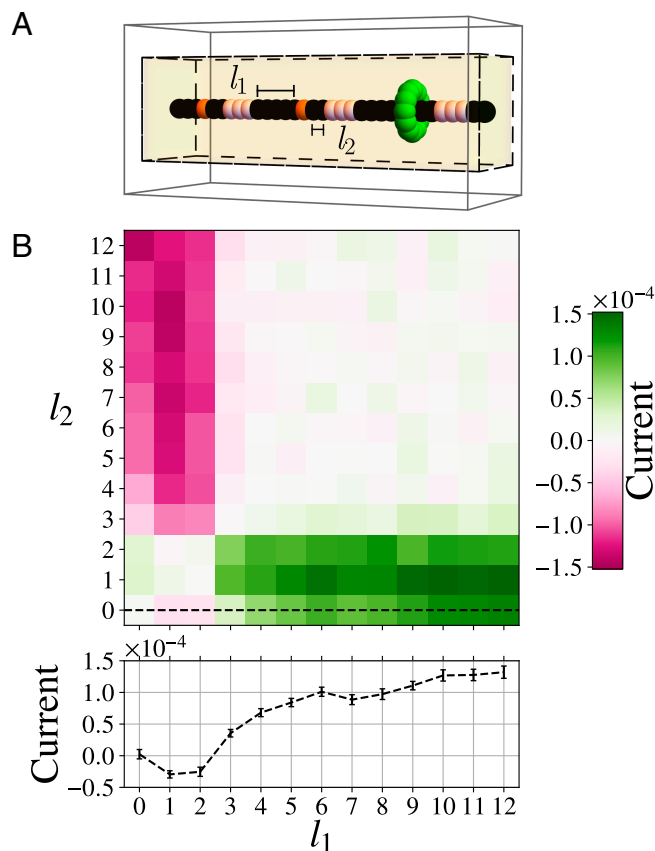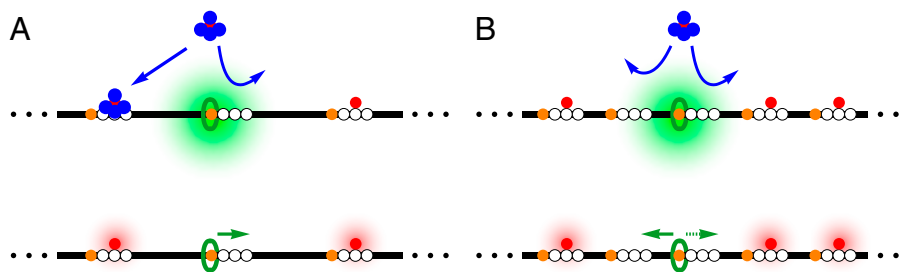
Fig. 3. The current reversal originates from a trade-off between two steric effects as the spacing l_1 decreases while $l_2 = 0$. (*Top Row*) Generation of blocking groups at catalytic sites is dominated by the attack of an FTC, the decomposition of which can leave behind a bound C. Steric repulsion from the shuttling ring (shaded green) shields either one (*A*) or two (*B*) catalytic sites from that attack depending on the l_1 spacing between motifs. Consequently, typical NESS configurations (*Bottom Row*) mirror the pattern of which sites are accessible to FTC (*Top Row*). In fact, the NESS's strong driving force from FTC to ETC + C imparts an arrow of time, implying that the configurations of the *Top Row* flow down into configurations of the *Bottom Row* much more than the reversed process. (*Bottom Row*) (*A*) At large l_1, the shuttling ring tends to be blocked from moving to the left, resulting in rightward motion. (*B*) At small l_1, the shuttling ring can move either right or left, but the binding site to the right is comparatively unstable due to a second steric effect between the shuttling ring and a bound C (shaded red).

it would be equally likely to see ETC and C coalesce into an FTC. That balance in the chemical reaction translates into a time-reversal symmetry for the shuttling ring—the forward and reversed trajectories are equally likely. The thermodynamic force from the driven FTC ⇌ ETC + C reaction breaks that symmetry. Due to the excess of FTC, C typically approaches the ring via one mechanism (extraction of C from FTC at a catalytic site) and departs via a different mechanism (loss of a solitary C with no tetrahedron nearby). When C is added and removed by a single time-reversed mechanism, the rates of those addition and removal events are coupled together; a faster binding rate also leads to a slower unbinding. With two mechanisms, however, fuel can be consumed to speed up the binding via the FTC decomposition without slowing the unbinding mechanism. The result for Fig. 3 is that configurations in the *Top Row* are rapidly pushed toward the *Bottom Row* without a balanced flow from the *Bottom Row* back up to the *Top Row*, allowing us to reason through the steps in sequence, i.e., first FTC approaches, then C is extracted to bind, and then a ring moves. That the driving force can break time-reversal symmetry to induce a shuttling-ring current is well known (23); the remarkable feature of the present model is that the sign of that current can flip due to subtle steric effects.

Other Steric Effects. While we have highlighted the current-reversal phenomenon as the most striking consequence of steric effects, other notable consequences manifest in Fig. 2. By symmetry, current must invert upon exchanging l_1 and l_2, so Fig. 2 is antisymmetric about $l_1 = l_2$. Without loss of generality, we focus on the data with $l_1 > l_2$. A prominent feature of Fig. 2 is that the current plummets when $l_2 \geq 3$, a length scale that corresponds to the effective range of repulsions between shuttling ring and ETC or FTC (*SI Appendix*, Fig. S7). If a binding site is more than three particle radii from a catalytic site, then the bound shuttling ring's dynamics becomes decoupled from catalytic decompositions that occur beyond the steric range.

A more subtle feature of Fig. 2 is that at fixed large l_1, the current depends nonmonotonically on the l_2 spacing. We just discussed why current drops when l_2 grows large relative to the shuttling ring's steric repulsions, but the data also show degrading performance when l_2 is made too small. Specifically, a larger current comes from the intermediate choice $l_2 = 1$ than from either $l_2 = 0$ or $l_2 = 2$. The schematic in Fig. 3 *A*, *Bottom Row* depicting such a large-l_1, $l_2 = 0$ regime, is useful to understand the cost of making l_2 too small. For the shuttling ring

to move rightward to the empty binding site, it will clash with the bound C, suggesting greater current with larger l_2. As in the current-reversal phenomenon, the nonmonotonicity of current for $l_2 = 0, 1, 2$ reflects a trade-off between competing effects. To maximize current, the spacing l_2 should be set to an intermediate value which is large enough but not too large.

The sensitivity of these "goldilocks" tradeoffs is especially stark in the regime with both $l_1 < 3$ and $l_2 < 3$. Within that regime, we see current reversal for $l_2 = 0$. Why does the current reversal disappear if l_2 is increased by one particle? That change slightly reduces the impact of the repulsion between shuttling ring and bound C that was highlighted in Fig. 3*B*. Because multiple steric effects act in opposition to each other, the net effect can be subtle and challenging to anticipate a priori. Indeed, our simulations of toy models are most appealing for their ability to highlight the tradeoffs that lead to distinct dynamics behaviors, not necessarily to anticipate a precise value of l_1 and l_2 that would induce an experimental current inversion. In similar ways, hard particles have been simulated to understand the qualitative structure of liquid crystal phase diagrams, although the simplifying model could never be expected to yield precise transition temperatures (27).

Validation from NESS Simulations. To more quantitatively evaluate the current-reversal mechanism, we coarse-grained NESS simulations for a $l_2 = 0$ linear motor into a kinetic model. We classified each microstate in the simulation into a mesostate based only on the presence or absence of a blocking group at each of the three catalytic sites, as depicted in Fig. 4. From these coarse-grained trajectories, we extracted the steady-state probability of each mesostate and the probability per unit time of transitioning between connected states, repeating the calculations for each l_1 spacing. With those measurements, we fit an l_1-dependent continuous-time Markov model for the mesostate kinetics. The Markov model serves as a concise way to consolidate mesoscopic kinetic measurements from NESS simulations, thereby illuminating how mesostate populations, rates, and currents change as l_1 is varied.

All those populations, rates, and currents are reported in *SI Appendix*, Fig. S4. We highlight in Fig. 4 those data most significant to quantitatively illustrate the mechanism of Fig. 3. Although the eight mesostates are defined by whether the three catalytic sites are blocked or unblocked, transitions between those states are not only induced by binding and unbinding of a blocking group (light red transitions). When the shuttling ring
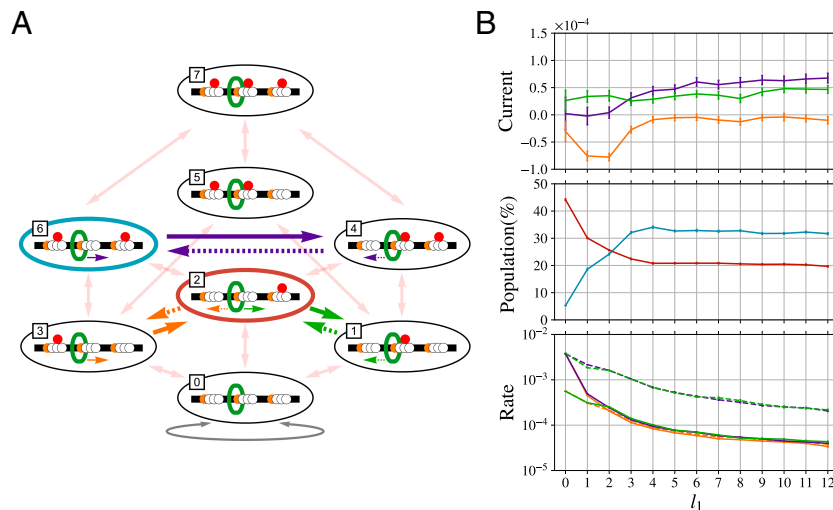
Fig. 4. (*A*) Simulated dynamics of the linear motor with three motifs can be coarse-grained onto an 8-state Markov model. The presence or absence of a blocking group at each of the three catalytic sites defines the eight states, and two of the most influential states are highlighted inside blue and red ovals. Transitions between states occur when a blocking group is added or removed (light red), when the shuttling ring moves on an unblocked track (gray), or when the shuttling ring moves on a partially blocked track (bold purple, orange, and green). As the generators of current, those purple, orange, and green transitions are highlighted, with solid arrows when the shuttling ring moves to the right (positive) and dashed arrows when it moves to the left (negative). (*B*) Selected data from the Markov model as a function of the l_1 spacing when $l_2 = 0$. (*Top*) The shuttling-ring current ($c_{ij}(l_1 + l_2 + 4)$) due to currents along the purple (c_{46}), orange (c_{32}), and green (c_{21}) edges. Summing these three contributions yields the total shuttling-ring current shown in Fig. 2 *B*, *Bottom*. (*Middle*) The empirical populations p_2 and p_6 for occupying states 2 (red) and 6 (blue). (*Bottom*) The rates of the highlighted transitions (k_{ij}) depicted in (*A*) with corresponding colors and line styles. Data for the states and transitions that are not highlighted are presented in *SI Appendix*, Figs. S4 and S6. Data points and error bars are given by the mean and standard error across 100 independent simulations with 2×10^8 time steps of size $\Delta t = 5 \times 10^{-3}$.

moves, it can also induce a change in the mesostate since the identities of the catalytic sites are defined relative to the shuttling ring. Fig. 4 highlights those mesostate transitions that correspond to shuttling ring motion, transitions colored purple, orange, and green. The net rightward shuttling ring current is the sum of those three currents, oriented in the direction of the solid arrows. Fig. 4 *B*, *Top* shows that the current reversal can largely be understood as a transition from dominance of the orange current at small l_1 to the purple current at large l_1.

The positive purple current and negative orange current are both amplified when the population of the originating mesostate increases. For example, increasing the steady-state probability of the mesostate drawn with a red boundary favors flux along the dashed orange transition and increasing the population of the mesostate drawn with a blue boundary favors flux along the solid purple transition. Fig. 4 *B*, *Middle* shows that the steady-state populations shift from the red to blue state as the spacing grows. That blue mesostate is more prevalent than the red at large l_1 because the high-fuel NESS introduces sufficient FTC to strongly favor configurations with more blocking groups. For small l_1, however, the population of the red state spikes; steric repulsion between the shuttling ring and the two nearest catalytic sites prevents blocking groups from attaching both to the left and right of the shuttling ring.

These measurements comport with the earlier qualitative steric arguments, placing the orange-to-purple current reversal on more quantitative grounds. It remains to explain why the negative orange current dominates over the positive green current since a high population of the red state gives a high flux along both the dashed orange and solid green transitions. As evidenced by the rates in Fig. 4*B*, there is a notable difference in the orange and green fluxes back into the red state. The rate of returning to the red state via leftward movement of the shuttling ring (dashed green) is far greater than the rate of returning to the red state via rightward movement of the shuttling ring (orange solid).

That dashed green transition originates from a highly unstable configuration with a shuttling ring adjacent to a blocking group whereas the solid orange transition originates from a state with an extra spacing l_1 between shuttling ring and blocking group. The overall effect, then, is that leftward movement becomes preferred at small spacing due to destabilizing steric interactions between the shuttling ring and blocking groups. The currents of Fig. 4 were computed by extracting both transition rates and populations from simulation. It is possible to estimate the current from the rates alone, taking the populations to be the steady state computed from the Markov model. That analysis, shown in *SI Appendix*, Fig. S5, generally tracks the measured populations of Fig. 4.

The Markov model analysis serves our purpose of validating the steric argument since the measured rates are useful and sufficient to illustrate kinetic asymmetry (22, 28). The model is thermodynamically grounded because the microscopic simulation's chemostats explicitly impose the thermodynamic driving force, through chemical potentials for FTC, ETC, and C. The impact of those chemical potentials on the Markov rates is not transparent, so those rates would need to be re-extracted from simulations when the chemical potentials are altered. By contrast, when working with the kinetics of elementary reactions, it is possible to simply relate the thermodynamic driving force to rates of transitioning forward and backward along a microscopically reversible elementary reaction (29–31). Such a connection between thermodynamics and Markov rates cannot be expected here since the transitions in Fig. 4 are coarse grained and combine together all of the different mechanisms to move between states into a single probability per unit time for each step (32). We therefore highlight that the Markov model should not be thought of as a model of the elementary kinetic steps. It should instead be understood as a coarse-grained kinetic model built upon a thermodynamically consistent microscopic simulation.

Discussion

We have illustrated a steric mechanism for current reversals of a specific catenane model. Of course, details of the model will quantitatively impact the transition, altering, for example, the particular distance l_1 at which a current reversal is induced, but our evidence suggests that the basic steric mechanism is very robust. *SI Appendix*, Fig. S1, shows the impact of driving the motor more strongly by tuning μ_{FTC} so as to induce more FTC fueling reactions to drive directed motion. For each l_1 spacing, the magnitude of the current grows with fuel concentration until saturation. The sign of that current does not depend on μ_{FTC}, so the current reversal persists whether operating in a weakly or strongly driven regime. The described simulations use a stochastic integrator to propagate an underdamped Langevin dynamics and *SI Appendix*, Fig. S3, furthermore shows that the current reversal is robust across a range of friction coefficients for the Langevin dynamics, strong evidence that the mechanism is not inertial in nature. A more detailed discussion of damping can be found in *SI Appendix*, section III, where we emphasize that the underdamped integrator can take the motor simulation well into the physically relevant overdamped regime. Compared to biological motors with Reynolds numbers of roughly $Re = 10^{-8}$ (20), we show that the main-text simulations correspond to Re on the order of 10^{-5} and those in *SI Appendix*, Fig. S3 approach Re of 10^{-9}.

We are still in the early days of being able to design molecular-scale machines that harvest free energy from their surroundings, particularly autonomous machines that mimic biological motors. To effectively design such machines we will need to identify design principles and effects that are robust across a range of conditions, such as driving force and friction. These principles should reveal what is required for molecular motors to approach thermodynamic limits when transducing fuel decomposition into directed motion (33). A significant challenge is that the operation of these machines can depend sensitively on the design, a dependence brought into focus by the current reversal. In light of that sensitivity, it is challenging to systematically engineer molecular motors. Whereas physicists have studied Brownian ratchet current reversals in response to variations in one or two parameters, e.g., a noise (34, 35) or driving frequency (36–38), biologists and chemists need ways to handle incredibly high dimensional design spaces. Protein motors can be mutated in any number of ways. Unconstrained by natural amino acids, supramolecular machines have even more conceivable variations.

Theory (39, 40) and simulation (41, 42) have important roles to parse the structure–function relationships in those supramolecular machines. Here, we have shown, through minimal models for NESS simulations, that the direction of a motor can be inverted by adjusting the spacing between binding sites and catalytic sites. Importantly, that sort of adjustment can be experimentally realized for supramolecular motors like those of refs. 13 and 14 by varying the length of alkane chains separating binding and catalytic sites. Our simulations are on a coarse-grained scale that does not seek to explicitly represent such atomistic dynamics. They are, nevertheless, sufficient to capture the steric hindrance, which has been shown to be important in other contexts, such as light-driven machines (43). For these light-driven molecular motors, precise control over the sterics can both increase and decrease the motor's speed (44).

We anticipate that the described current reversal mechanism will be relevant to many flavors of artificial molecular motors (45), particularly to those applications which require tracks to direct molecular motors (46). The rotary motor of ref. 13 involved a circular track, but in our simulations, the track could be unfurled into a linear track without disturbing the essential behavior. That linear configuration was introduced here as a means of isolating the origin of the current reversal, but the linear motor can also be useful in its own right. Whether built from DNA components (47, 48) or supramolecular chemistry, synthetic motors walking along linear tracks could form the basis for nanoscale assembly lines, molecular robots, and active materials (26). Hopefully, the simulations and mechanisms described here will prove useful in designing those future generations of synthetic motors.

Materials and Methods

Langevin Dynamics with Chemostats. As described in more detail in *SI Appendix*, section VI, the motor and its surroundings were simulated with underdamped Langevin dynamics while the concentrations of FTC, ETC, and C were maintained by grand canonical Monte Carlo chemostats (49–51). This merging of Langevin dynamics with chemostats was achieved by confining the motor to an inner box, which was permeable to the FTC, ETC , and C particles but not to the motor (22). Fuel and waste diffused in and out of the inner box sufficiently quickly that the concentrations experienced by the motor reflect the chemical potentials imposed by Monte Carlo insertion and deletion moves in an outer box. This construction for the rotary motor is depicted in Fig. 1*B* and for the linear motor in Fig. 2*A*. Whether in the inner or outer box, the ith particle with position $\mathbf{r}_i$ and momentum $\mathbf{p}_i$ was evolved in time according to the underdamped Langevin equation:

$$\dot{\mathbf{r}}_i = \frac{\mathbf{p}_i}{m_i}$$
$$\dot{\mathbf{p}}_i = -\frac{\partial U(\mathbf{r})}{\partial \mathbf{r}_i} - \frac{\gamma}{m_i}\mathbf{p}_i + \boldsymbol{\xi}_i, \qquad [1]$$

where the potential energy U is a function of all positions $\mathbf{r}$, m_i is the particle's mass, γ is the friction coefficient and $\boldsymbol{\xi}$ is a white noise satisfying $\langle\boldsymbol{\xi}_i\rangle = \mathbf{0}$ and $\langle\boldsymbol{\xi}_i(t)\boldsymbol{\xi}_j(t')\rangle = 2\gamma k_B T\delta(t - t')\delta_{ij}\mathbf{I}$ at temperature T, where $\mathbf{I}$ is the identity matrix. This equation was numerically integrated with a time step Δt (52), described in more detail in *SI Appendix, section VI*. Simulations reported in the main text were carried out using nondimensionalized units (Boltzmann constant $k_B = 1$) with $T = 0.5$, $\Delta t = 5 \times 10^{-3}$, and $\gamma = 0.5$. GCMC moves are attempted every 100 Langevin time steps.

Modeling Interactions. The motor design is determined by the spacing of various types of beads comprising binding sites, catalytic sites, etc. The details of the interactions between those beads also strongly impact the behavior of the motor. Here, we closely followed our prior design of a minimal motor model (22), with specific modeling details discussed in *SI Appendix*, section VI. Briefly, the motor rings are made up of beads linked together with finitely extensible nonlinear elastic (FENE) bonds, with a three-body angular potential enforcing circular rings. The tetrahedral clusters, depicted in blue, present in both FTC and ETC are held together with harmonic bonds. All particles, those in the motor and those in the fuel/waste, additionally interact with all other particles via two-body 12-6 Lennard–Jones interactions, but with coefficients for the 12-term (ϵ_R) and 6-term (ϵ_A) independently controlled to separately tune repulsions and attractions, respectively. Holding fixed the strengths of the bonded interactions, the motor/fuel system is designed by choosing appropriate attraction and repulsion strengths between all pairs of particle types. Those particle types can be identified from the snapshot images–different colors are different particle types, but with an important caveat. The colors actually distinguish the functional role of different particles, not the particle type. For example, although the four particles that make up a tetrahedral cluster are all colored blue, they represent four distinct particle types (TET1, TET2, TET3, and TET4) with distinct pairwise interaction strengths. Where possible, we matched all interactions with our prior work (22), but we made one important modification to the white catalytic site. In the earlier work, that catalytic site had three distinct particle types, a CAT2 particle bonded to a CAT1 particle bonded to a CAT3

particle, each of which was rendered white. To ensure that the model would be symmetric when l_1 and l_2 were permuted, it became necessary to reparameterize a symmetric catalytic site built from a CAT2 particle bonded to a CAT1 bonded to another CAT2, with pairwise interaction strengths provided in *SI Appendix,* Table S3.

Coarse Graining and Markov State Model. The continuous-time Markov model of Fig. 4*A* was parameterized from NESS simulation data. Coarse graining was performed in two stages: first by mapping each microstate onto one of 24 mesostates (the "lab frame") and then by clumping together groups of three symmetrically equivalent states that have identical blocking group configurations relative to the position of the shuttling ring (the "relative frame"). The coarse graining in the lab frame used mesostates based on the position of the shuttling ring and the presence or absence of a blocking group at each of the three catalytic sites. To determine whether a catalytic site was blocked or not, we calculated the distance between the middle catalytic particle and all free C particles in the system. If at least one C particle was within 1.2 distance units of the middle particle of a catalytic site then the site was considered to be blocked. The shuttling ring location was determined from a core set coarse graining (53, 54). We calculated which linear track particle was closest to the shuttling ring center of mass. If the closest track particle was a binding site, that binding site was considered to be the current position of the shuttling ring. Otherwise, the position was considered to be the last visited binding site. Three catalytic sites can be blocked or unblocked and the ring can reside at one of three possible binding sites, leading to 24 different mesostates in the lab frame.

Taking into account the translational symmetry, it suffices to track the motion in the relative frame measured with respect to the shuttling ring. Dynamics in the relative frame moves between the 8 states depicted in Fig. 4*A*. In building the relative-frame Markov model, we represented the probability of each of the 8 states as a vector $\mathbf{p} = [p_0, p_1, p_2, p_3, p_4, p_5, p_6, p_7]^T$, with states numbered as indicated in Fig. 4. The probability evolves according to the master equation

$$\frac{d\mathbf{p}}{dt} = \mathbf{W}\mathbf{p},\qquad [2]$$

where $\mathbf{W}$ is the continuous-time rate matrix

$$\mathbf{W} = \begin{bmatrix} -\Sigma_0 & k_{10} & k_{20} & k_{30} & 0 & 0 & 0 & 0 \\ k_{01} & -\Sigma_1 & k_{21} & 0 & k_{41} & k_{51} & 0 & 0 \\ k_{02} & k_{12} & -\Sigma_2 & k_{32} & k_{42} & 0 & k_{62} & 0 \\ k_{03} & 0 & k_{23} & -\Sigma_3 & 0 & k_{53} & k_{63} & 0 \\ 0 & k_{14} & k_{24} & 0 & -\Sigma_4 & 0 & k_{64} & k_{74} \\ 0 & k_{15} & 0 & k_{35} & 0 & -\Sigma_5 & 0 & k_{75} \\ 0 & 0 & k_{26} & k_{36} & k_{46} & 0 & -\Sigma_6 & k_{76} \\ 0 & 0 & 0 & 0 & k_{47} & k_{57} & k_{67} & -\Sigma_7 \end{bmatrix}.$$
$$[3]$$

In choosing this form of the rate matrix, we assume that transitions not drawn in the network of Fig. 4 have zero rates. In reality, the simulated system is soft and very occasionally it may be possible that a shuttling ring squeezes past a blocking group. Because such transitions were so exceedingly rare, the Markov model treated those events as having zero rates. We write the total time spent

in state i as τ_i and the total number of transitions from i to j as N_{ij}, allowing us to estimate the nonzero rates as

$$k_{ij} = \frac{N_{ij}}{\tau_i}.\qquad [4]$$

Along the diagonal of the rate matrix are the total escape rates from state i, $\Sigma_i \equiv \sum_{j\neq i} k_{ij}$. At steady state, $\frac{d\mathbf{p}}{dt} = \mathbf{0}$, and the steady-state population of states is given by $\boldsymbol{\pi}$ equal to the normalized top eigenvector of $\mathbf{W}$. The net steady-state probability current along an individual edge connecting states i and j is given by

$$\tilde{c}_{ij} = \pi_i k_{ij} - \pi_j k_{ji}.\qquad [5]$$

The Markov model's steady-state density can differ slightly from the empirical density (this could happen due to finite-sampling effects, a breakdown of the Markov assumption, or if the disallowed transitions did not truly have zero rates), so we additionally measure the empirical density of each state as the fraction of time spent in that state:

$$p_i = \frac{\tau_i}{\tau},\qquad [6]$$

where $\tau = N_{\text{steps}}\Delta t$ is the total simulated time. Since the simulations provide access to both empirical densities and rate estimates, We find that current calculations tend to be most robust when we incorporate information from both the empirical densities and the rate estimates (*SI Appendix,* section IV). To do so, we compute the current associated with the empirical density

$$c_{ij} = p_i k_{ij} - p_j k_{ji},\qquad [7]$$

for every edge of the 8-state relative-frame Markov model.

We note that in the relative frame of reference, the shuttling ring remains fixed, yet transitions depicted with large purple, orange, green, and gray lines in Fig. 4 correspond to transitions where the shuttling ring moves in the lab frame. We can therefore deduce the lab-frame current from the probability per unit time flowing across those purple, orange, and green edges of the relative-frame Markov model. Since the shuttling ring will pass $l_1 + l_2 + 4$ sites upon moving from one binding site to the next, the net shuttling ring current (displacement per unit time) is thus $(l_1 + l_2 + 4)(c_{64} + c_{32} + c_{21})$. That total current is readily decomposed into the contributions coming from the purple (c_{46}), orange (c_{32}), and green (c_{21}) edges, as illustrated in Fig. 4. The other transitions in the Markov model (depicted by thin red arrows in Fig. 4) correspond to blocking group creation and removal, with no corresponding shuttling ring movement, and therefore do not contribute to the physical movement of the shuttling ring and corresponding current. Fig. 4*B* gives data for a select number of states and rates, with the full dataset presented in *SI Appendix,* Fig. S4.

1. A. I. Brown, D. A. Sivak, Toward the design principles of molecular machines. *Phys. Can.* **73**, 61–66 (2017).
2. A. B. Kolomeisky, M. E. Fisher, Molecular motors: A theorist's perspective. *Annu. Rev. Phys. Chem.* **58**, 675–695 (2007).
3. M. L. Mugnai, C. Hyeon, M. Hinczewski, D. Thirumalai, Theoretical perspectives on biological machines. *Rev. Mod. Phys.* **92**, 025001 (2020).
4. B. J. Schnapp, T. S. Reese, Dynein is the motor for retrograde axonal transport of organelles. *Proc. Natl. Acad. Sci. U.S.A.* **86**, 1548–1552 (1989).
5. J. Howard, A. Hudspeth, R. Vale, Movement of microtubules by single kinesin molecules. *Nature* **342**, 154–158 (1989).
6. J. T. Finer, R. M. Simmons, J. A. Spudich, Single myosin molecule mechanics: Piconewton forces and nanometre steps. *Nature* **368**, 113–119 (1994).
7. H. Noji, R. Yasuda, M. Yoshida, K. Kinosita, Direct observation of the rotation of F1-ATPase. *Nature* **386**, 299–302 (1997).
8. Z. Bryant, D. Altman, J. A. Spudich, The power stroke of myosin VI and the basis of reverse directionality. *Proc. Natl. Acad. Sci. U.S.A.* **104**, 772–777 (2007).
9. F. Buss, G. Spudich, J. Kendrick-Jones, Myosin VI: Cellular functions and motor properties. *Annu. Rev. Cell Dev. Biol.* **20**, 649–676 (2004).
10. J. C. Liao, M. W. Elting, S. L. Delp, J. A. Spudich, Z. Bryant, Engineered myosin VI motors reveal minimal structural determinants of directionality and processivity. *J. Mol. Biol.* **392**, 862–867 (2009).
11. E. P. Sablin *et al.*, Direction determination in the minus-end-directed kinesin motor ncd. *Nature* **395**, 813–816 (1998).
12. S. Can, S. Lacey, M. Gur, A. P. Carter, A. Yildiz, Directionality of dynein is controlled by the angle and length of its stalk. *Nature* **566**, 407–410 (2019).
13. M. R. Wilson *et al.*, An autonomous chemically fuelled small-molecule motor. *Nature* **534**, 235–240 (2016).
14. S. Borsley, D. A. Leigh, B. M. Roberts, A doubly kinetically-gated information ratchet autonomously driven by carbodiimide hydration. *J. Am. Chem. Soc.* **143**, 4414–4420 (2021).
15. S. Borsley, E. Kreidt, D. A. Leigh, B. M. Roberts, Autonomous fuelled directional rotation about a covalent single bond. *Nature* **604**, 80–85 (2022).

16. T. R. Kline, W. F. Paxton, T. E. Mallouk, A. Sen, Catalytic nanomotors: Remote-controlled autonomous movement of striped metallic nanorods. *Angew. Chem. Int. Ed.* **44**, 744–746 (2005).

17. A. A. Solovev, S. Sanchez, M. Pumera, Y. F. Mei, O. G. Schmidt, Magnetic control of tubular catalytic microbots for the transport, assembly, and delivery of micro-objects. *Adv. Func. Mater.* **20**, 2430–2435 (2010).

18. C. Bustamante, D. Keller, G. Oster, The physics of molecular motors. *Acc. Chem. Res.* **34**, 412–420 (2001).

19. R. D. Astumian, Design principles for Brownian molecular machines: How to swim in molasses and walk in a hurricane. *Phys. Chem. Chem. Phys.* **9**, 5067–5083 (2007).

20. A. I. Brown, D. A. Sivak, Theory of nonequilibrium free energy transduction by molecular machines. *Chem. Rev.* **120**, 434–459 (2019).

21. D. Lacoste, A. Lau, K. Mallick, Fluctuation theorem and large deviation function for a solvable model of a molecular motor. *Phys. Rev. E* **1**, 011915 (2008).

22. A. Albaugh, T. R. Gingrich, Simulating a chemically fueled molecular motor with nonequilibrium molecular dynamics. *Nat. Commun.* **13**, 2204 (2022).

23. R. D. Astumian, Running on information. *Nat. Nanotechnol.* **11**, 582–583 (2016).

24. D. A. Leigh, J. K. Wong, F. Dehez, F. Zerbetto, Unidirectional rotation in a mechanically interlocked molecular rotor. *Nature* **424**, 174–179 (2003).

25. A. Albaugh, T. R. Gingrich, Estimating reciprocal partition functions to enable design space sampling. *J. Chem. Phys.* **153**, 204102 (2020).

26. Z. Wang, R. Hou, I. Y. Loh, Track-walking molecular motors: A new generation beyond bridge-burning designs. *Nanoscale* **11**, 9240–9263 (2019).

27. M. P. Allen, Simulations using hard particles. *Philos. Trans. Roy. Soc. London Ser. A: Phys. Eng. Sci.* **344**, 323–337 (1993).

28. E. Penocchio, G. Ragazzon, Kinetic barrier diagrams to visualize and engineer molecular nonequilibrium systems. *Small* **19**, 2206188 (2023).

29. M. Bauer, F. Cornu, Local detailed balance: A microscopic derivation. *J. Phys. A: Math. Theor.* **48**, 015008 (2014).

30. R. D. Astumian, Trajectory and cycle-based thermodynamics and kinetics of molecular machines: The importance of microscopic reversibility. *Acc. Chem. Res.* **51**, 2653–2661 (2018).

31. G. Falasco, M. Esposito, Local detailed balance across scales: From diffusions to jump processes and beyond. *Phys. Rev. E* **103**, 042114 (2021).

32. M. Esposito, Stochastic thermodynamics under coarse graining. *Phys. Rev. E* **85**, 041125 (2012).

33. A. Albaugh, R.-S. Fu, G. Gu, T. R. Gingrich, Limits on the precision of catenane molecular motors: Insights from thermodynamics and molecular dynamics simulations. arXiv [Preprint] (2023). http://arxiv.org/abs/2306.03182 (Accessed 17 July 2023).

34. C. R. Doering, W. Horsthemke, J. Riordan, Nonequilibrium fluctuation-induced transport. *Phys. Rev. Lett.* **72**, 2984 (1994).

35. J. Kula, T. Czernik, J. Łuczka, Brownian ratchets: Transport controlled by thermal noise. *Phys. Rev. Lett.* **80**, 1377 (1998).

36. R. Bartussek, P. Hänggi, J. G. Kissner, Periodically rocked thermal ratchets. *EPL (Europhys. Lett.)* **28**, 459 (1994).

37. A. Wickenbrock, D. Cubero, N. A. Wahab, P. Phoonthong, F. Renzoni, Current reversals in a rocking ratchet: The frequency domain. *Phys. Rev. E* **84**, 021127 (2011).

38. N. E. Strand, R. S. Fu, T. R. Gingrich, Current inversion in a periodically driven two-dimensional Brownian ratchet. *Phys. Rev. E* **102**, 012141 (2020).

39. S. Amano, S. Borsley, D. A. Leigh, Z. Sun, Chemical engines: Driving systems away from equilibrium through catalyst reaction cycles. *Nat. Nanotechnol.* **16**, 1057–1067 (2021).

40. S. Amano et al., Insights from an information thermodynamics analysis of a synthetic molecular motor. *Nat. Chem.* **14**, 530–537 (2022).

41. C. S. Korosec et al., Substrate stiffness tunes the dynamics of polyvalent rolling motors. *Soft Matter* **17**, 1468–1479 (2021).

42. A. Courbet et al., Computational design of mechanically coupled axle-rotor protein assemblies. *Science* **376**, 383–390 (2022).

43. D. Roke, S. J. Wezenberg, B. L. Feringa, Molecular rotary motors: Unidirectional motion around double bonds. *Proc. Natl. Acad. Sci. U.S.A.* **115**, 9423–9431 (2018).

44. L. A. Huber et al., Steric effects on the thermal processes of hemithioindigo based molecular motor rotation. *Chem. -A Eur. J.* **27**, 10758–10765 (2021).

45. S. Erbas-Cakmak, D. A. Leigh, C. T. McTernan, A. L. Nussbaumer, Artificial molecular machines. *Chem. Rev.* **115**, 10081–10206 (2015).

46. I. N. Unksov et al., Through the eyes of creators: Observing artificial molecular motors. *ACS Nanosci. Au* **2**, 140–159 (2022).

47. J. Bath, S. J. Green, K. E. Allen, A. J. Turberfield, Mechanism for a directional, processive, and reversible DNA motor. *Small* **5**, 1513–1516 (2009).

48. M. Liu et al., Biomimetic autonomous enzymatic nanowalker of high fuel efficiency. *ACS Nano* **10**, 5882–5890 (2016).

49. D. Frenkel, B. Smit, *Understanding Molecular Simulation: From Algorithms to Applications* (Elsevier, ed. 1, 2001).

50. A. Gupta, L. A. Clark, R. Q. Snurr, Grand canonical Monte Carlo simulations of nonrigid molecules: Siting and segregation in silicalite zeolite. *Langmuir* **16**, 3910–3919 (2000).

51. S. Chempath, L. A. Clark, R. Q. Snurr, Two general methods for grand canonical ensemble simulation of molecules with internal flexibility. *J. Chem. Phys.* **118**, 7635–7643 (2003).

52. J. Fass et al., Quantifying configuration-sampling error in Langevin simulations of complex molecular systems. *Entropy* **20**, 318 (2018).

53. N. V. Buchete, G. Hummer, Coarse master equations for peptide folding dynamics. *J. Phys. Chem. B* **112**, 6057–6069 (2008).

54. C. Schütte, F. Noé, J. Lu, M. Sarich, E. Vanden-Eijnden, Markov state models based on milestoning. *J. Chem. Phys.* **134**, 204105 (2011).

55. A. Albaugh, G. Gu, T. Gingrich, Sterically driven current reversal in a molecular motor model. Zenodo. https://zenodo.org/record/6712829. Deposited 23 June 2023.